



Core-shell structured $\text{Ni}_{12}\text{P}_5/\text{Ni}_3(\text{PO}_4)_2$ hollow spheres as difunctional and efficient electrocatalysts for overall water electrolysis



Jinfa Chang ^{a,c}, Qing Lv ^{a,c}, Guoqiang Li ^{a,c}, Junjie Ge ^b, Changpeng Liu ^{b,*}, Wei Xing ^{a,*}

^a State Key Laboratory of Electroanalytical Chemistry, Changchun Institute of Applied Chemistry, 5625 Renmin Street, Changchun 130022, PR China

^b Laboratory of Advanced Power Sources, Jilin Province Key Laboratory of Low Carbon Chemical Power Sources, Changchun Institute of Applied Chemistry, 5625 Renmin Street, Changchun 130022, PR China

^c University of Chinese Academy of Sciences, Beijing 100039, PR China

ARTICLE INFO

Article history:

Received 4 March 2016

Received in revised form 18 October 2016

Accepted 23 November 2016

Available online 24 November 2016

Keywords:

Core-shell structure

Nickel phosphide

Nickel phosphate

Bifunctional catalysts

Overall water splitting

ABSTRACT

Non-precious metal catalysts for hydrogen evolution reaction (HER) and oxygen evolution reaction (OER) are the cost-effective materials for overall water splitting. Here, we report that the core-shell structured $\text{Ni}_{12}\text{P}_5/\text{Ni}_3(\text{PO}_4)_2$ hollow spheres ($\text{Ni}_{12}\text{P}_5/\text{Ni}_3(\text{PO}_4)_2\text{-HS}$) exhibits high activity and stability towards both HER and OER in strong alkaline media. A current density of 10 mA cm^{-2} is generated at an overpotential of 0.114 V and 0.318 V in 1 M KOH for HER and OER, respectively. The high activity is attributed to the hollow core-shell ($\text{Ni}_{12}\text{P}_5/\text{Ni}_3(\text{PO}_4)_2$) structure that the material adopts under catalytic conditions. The $\text{Ni}_{12}\text{P}_5/\text{Ni}_3(\text{PO}_4)_2\text{-HS}$ can serve as both cathode and anode catalysts for a real water electrolysis cell, which generates a current density of 357.6 mA cm^{-2} at 1.8 V and stable at 300 mA cm^{-2} for at least 100 h , the potential catalytic degradation mechanism has been systematically studied and discussed.

© 2016 Elsevier B.V. All rights reserved.

1. Introduction

Hydrogen energy is attracting more and more attention as a clean and renewable energy because of its great potential in replacing the petroleum based energy source [1–3]. However, H_2 is only an energy carrier rather than energy source since it needs to be extracted from organic molecules or water. Today, most H_2 is produced through the nickel-catalyzed conversion of CH_4 [4], where CO/CO_2 are formed as byproducts and the poisonous/greenhouse gases make the technique environmentally less attractive. Water electrolysis is a far cleaner route since only H_2 and O_2 are generated during the electrolytic process [2,5,6]. Nevertheless, water electrolysis requires the utilization of precious metals (Pt) or noble metal oxides (RuO_2 and IrO_2) as catalysts to facilitate the hydrogen and oxygen evolution reactions [7–9]. The high cost and scarcity of these precious materials make them less attractive in mass production of water electrolyser (WE). Thus, to make the H_2 production from electrolysis economically more competitive, it is desirable to develop inexpensive, earth-abundant WE electrocatalysts with high efficiency [10,11]. Since Lewis's group found that Ni_2P is a new earth-abundant HER catalyst in 2013 [12], transition-metal

sulfides [13–16], selenides [17,18], phosphides [19–21], carbides [22], borides [23] and even non-metal materials [24] were shown as efficient catalysts for HER in strong acidic electrolytes to replace the commonly used precious Pt catalysts. On the OER side, catalysts based on the oxides/hydroxides of cobalt [25,26], nickel [27,28], manganese [29,30], iron [31,32], and copper [33,34] were found to process excellent OER catalytic activities under basic conditions. However, to accomplish overall water electrolysis, the coupling of HER and OER catalysts in the same electrolyte is desirable. Until now, very few catalysts are capable of catalyzing both HER and OER in the same media in despite of the significant progress made [35–39]. In the past two years, a variety of Ni-P HER catalysts with different stoichiometries, such as NiP_2 [40], Ni_2P [41], Ni_5P_4 [42], and N_{12}P_5 [43,44] have been reported, and their catalytic performances toward HER were carefully investigated. However, the systematic study of Ni-P catalysts for OER and overall water splitting was inadequate. Recently, Ni_2P , previously known for its excellent catalytic behavior for HER, has been shown as effective OER catalyst in 1 M KOH , and the high activity for OER was attributed to the core-shell ($\text{Ni}_2\text{P}/\text{NiO}_x$) structure [37]. However, the catalyst evaluation was only conducted in half cell, where the current density was too low for realistic situation. Therefore, it is of significant importance to design and synthesis bifunctional catalysts that are able to deliver high performance in a real water electrolysis cell. Furthermore, for the application of catalysts based

* Corresponding authors.

E-mail addresses: liuchp@ciac.ac.cn (C. Liu), xingwei@ciac.ac.cn (W. Xing).

on phosphide, the most pressing need is to study their long term stability, where the degradation mechanism at high current density/high potential during operation is highly valuable.

Herein, we report a one-pot, facile solvothermal reaction method to synthesis core-shell structured $\text{Ni}_{12}\text{P}_5/\text{Ni}_3(\text{PO}_4)_2$ -HS for overall water splitting. The as-prepared $\text{Ni}_{12}\text{P}_5/\text{Ni}_3(\text{PO}_4)_2$ -HS can be directly utilized as electrocatalysts for both HER and OER in strong alkaline electrolyte, achieving a current density of 10 mA cm^{-2} with overpotentials at 0.114 V for HER and 0.318 V for OER, respectively. Furthermore, when integrated into a practical anion exchange membrane water electrolyser (AEMWE), a current density of 357.6 mA cm^{-2} was acquired at 1.8 V , which is rather competitive to the cell using IrO_2 anode and Pt black cathode, showing the promising nature of $\text{Ni}_{12}\text{P}_5/\text{Ni}_3(\text{PO}_4)_2$ -HS in acting as a non-noble bifunctional catalyst. What's more, the potential catalytic degradation mechanism has been systematic studied and discussed by various characterizations, such as XRD, SEM, TEM and XPS. The results indicate that $\text{Ni}_{12}\text{P}_5/\text{Ni}_3(\text{PO}_4)_2$ -HS are promising to replace the precious metals and noble metal oxides catalysts in the electrochemical water electrolytic devices.

2. Experimental section

2.1. Materials

Sodium hypophosphite monohydrate ($\geq 99.0\%$, $\text{NaH}_2\text{PO}_2\cdot\text{H}_2\text{O}$), sodium dihydrogen phosphate ($\geq 99.0\%$, $\text{NaH}_2\text{PO}_4\cdot 2\text{H}_2\text{O}$), nickel sulfate hexahydrate ($\geq 98.0\%$, $\text{NiSO}_4\cdot 6\text{H}_2\text{O}$), nickel chloride hexahydrate puratrem ($\geq 99.0\%$, $\text{NiCl}_2\cdot 6\text{H}_2\text{O}$), iridium oxide nanoparticles (IrO_2) and Pt/C (20%) were purchased from Aldrich Chemical Co. (USA). Nafion solution (5%) and PTFE (10%) was purchased from Dupont Co. (USA). CTAB, *n*-butanol, cyclohexane, potassium hydroxide ($\geq 95.0\%$, KOH) and ethanol ($\geq 99.7\%$) were purchased from Beijing Chemical Co. (China). All the chemicals were of analytical grade and used as received. Highly purified N_2 and O_2 were supplied by Changchun Juyang Co Ltd. Ultrapure water (resistivity: $\rho \geq 18\text{ M}\Omega\text{ cm}$) was used to prepare the solutions.

2.2. Synthesis of $\text{Ni}_{12}\text{P}_5/\text{Ni}_3(\text{PO}_4)_2$ -HS

The $\text{Ni}_{12}\text{P}_5/\text{Ni}_3(\text{PO}_4)_2$ -HS were prepared by a water-in-oil microemulsion method which was prepared by using CTAB as surfactant and *n*-butanol as co-surfactant [45]. In a typical experimental procedure, 1 mmol $\text{NaH}_2\text{PO}_2\cdot\text{H}_2\text{O}$ and 2.5 mmol $\text{NiSO}_4\cdot 6\text{H}_2\text{O}$ were dissolved in distilled water to form a 6 mL solution. Then 14 mL cyclohexane, 20 mmol CTAB and 10 mL *n*-butanol were added. The mixture was vigorously stirred with a magnetic pulsator at room temperature until a transparent microemulsion was obtained. The as-prepared microemulsions were poured into Teflon-lined stainless steel autoclaves and maintained at $150\text{ }^\circ\text{C}$ for 12 h before being cooled to room temperature naturally. The black products were collected, washed with distilled water several times and dried in air at $50\text{ }^\circ\text{C}$ for 4 h, then $\text{Ni}_{12}\text{P}_5/\text{Ni}_3(\text{PO}_4)_2$ -HS was obtained.

For comparison, Core-shell structured $\text{Ni}_{12}\text{P}_5/\text{Ni}_3(\text{PO}_4)_2$ solid spheres ($\text{Ni}_{12}\text{P}_5/\text{Ni}_3(\text{PO}_4)_2$ -SS) were prepared in a simple aqueous solution only containing $\text{NaH}_2\text{PO}_2\cdot\text{H}_2\text{O}$ and $\text{NiSO}_4\cdot 6\text{H}_2\text{O}$ with the same concentration as above by the hydrothermal route at $150\text{ }^\circ\text{C}$ for 12 h.

The bulk $\text{Ni}_3(\text{PO}_4)_2$ was prepared by aqueous solution method as follows: 1 mmol $\text{NaH}_2\text{PO}_4\cdot 2\text{H}_2\text{O}$ and 1.5 mmol $\text{NiCl}_2\cdot 6\text{H}_2\text{O}$ were dissolved in distilled water under stirring, the pH of above solution was adjust to 7.6, after centrifugal separation washing with water

three times, the $\text{Ni}_3(\text{PO}_4)_2$ was collected and vacuum drying, the bulk $\text{Ni}_3(\text{PO}_4)_2$ was obtained.

2.3. Physical characterizations

Scanning electron microscopy (SEM) measurements were performed with an XL 30 ESEM FEG field emission scanning electron microscope. Transmission electron microscopy (TEM), high resolution transmission electron microscopy (HR-TEM), high-annular dark-field scanning transmission electron microscopy (STEM) and element mapping analysis were conducted on Philips TECNAI G2 electron microscope operating at 200 kV. X-ray diffraction (XRD) measurements were performed with a PW-1700 diffractometer using a $\text{Cu K}\alpha$ ($\lambda = 1.5405\text{ \AA}$) radiation source (Philips Co.). The textural and morphological features of the $\text{Ni}_{12}\text{P}_5/\text{Ni}_3(\text{PO}_4)_2$ -HS were determined by nitrogen physisorption at 77 K in a Micromeritics ASAP 2020. Textural properties such as the specific surface area pore volume and pore size distribution were calculated from each corresponding nitrogen adsorption–desorption isotherm, applying the Brunauer–Emmett–Teller (BET) equation and the Barrett–Joyner–Halenda (BJH). X-ray photoelectron spectroscopy (XPS) measurements were carried out on $\text{Mg K}\alpha$ radiation source (Kratos XSAM-800 spectrometer). The bulk compositions were evaluated by inductively coupled plasma optical emission spectrometer (ICP-OES, X Series 2, Thermo Scientific USA).

In order to probe and compare the electrical resistance of as prepared $\text{Ni}_{12}\text{P}_5/\text{Ni}_3(\text{PO}_4)_2$ -HS, $\text{Ni}_{12}\text{P}_5/\text{Ni}_3(\text{PO}_4)_2$ -SS and bulk $\text{Ni}_3(\text{PO}_4)_2$, a typical four-probe method (performed on a KDY-1-type four-probe resistivity/square resistance tester, Guangzhou KunDe Co., Ltd., China) was used, and measurements were taken at ambient temperature (ca. $25\text{ }^\circ\text{C}$) [46]. Typically, the powder samples were pressed into pellets with diameters of 10 mm and thicknesses of approximately 3 mm under a pressure of $4.9 \times 10^8\text{ Pa}$. Each sample was tested five times, and the average value was reported.

2.4. Electrochemical measurements

Electrochemical measurements were performed with EG & G PARSTAT 4000 potentiostat/galvanostat (Princeton Applied Research Co., USA). A conventional one-component three-electrode cell was used, including a glassy carbon electrode (GCE, geometric area = 0.07 cm^2) as the working electrode, a platinum foil was used as the auxiliary electrode and a mercuric oxide (Hg/HgO , 1 M KOH) electrode was used as the reference electrode. To prepare the working electrode, 5 mg of the catalyst (for the bulk $\text{Ni}_3(\text{PO}_4)_2$ sample, in order to enhance the electroconductibility, it was physically mixed with Vulcan XC-72 active carbon with a mass ratio of 1:1) and 100 μL of 5 wt% Nafion solution were dispersed in 900 mL of ethanol solvent, followed by ultrasounded at least 30 min. Then 10 μL of the ink was dropped onto a GCE (\sim loading: 0.71 mg cm^{-2}). For the HER and OER reactions, the electrolyte (1 M KOH) was degassed by bubbling N_2 or O_2 for at least 30 minutes before the electrochemical measurements. Prior recording the HER and OER activity of all samples, the catalysts were activated by 20 CV scans along the potential window of -0.8 to -1.1 V vs. Hg/HgO for HER (0.3 – 0.9 V vs. Hg/HgO for OER) in 1 M KOH at a scan rate of 100 mV s^{-1} , then the linear sweep voltammetry (LSV) with a scan rate of 5 mV s^{-1} was performed. All the potentials reported in our work were vs. the reversible hydrogen electrode (RHE). In 1 M KOH ($\text{pH} = 13.61$), $E(\text{RHE}) = E(\text{Hg}/\text{HgO}) + 0.059 * \text{pH} = 0.098\text{ V} + 0.059\text{ V} * \text{pH} = 0.901\text{ V}$. Ohmic drop was corrected using electrochemical impedance spectroscopy (EIS) methods according to the equation: $E_a = E_b - IR_s$, where E_a is the overpotential after I - R correction, E_b is the overpotential before I - R correction, I is the corresponding current and R_s is the resistance of the system obtained from EIS plots as the

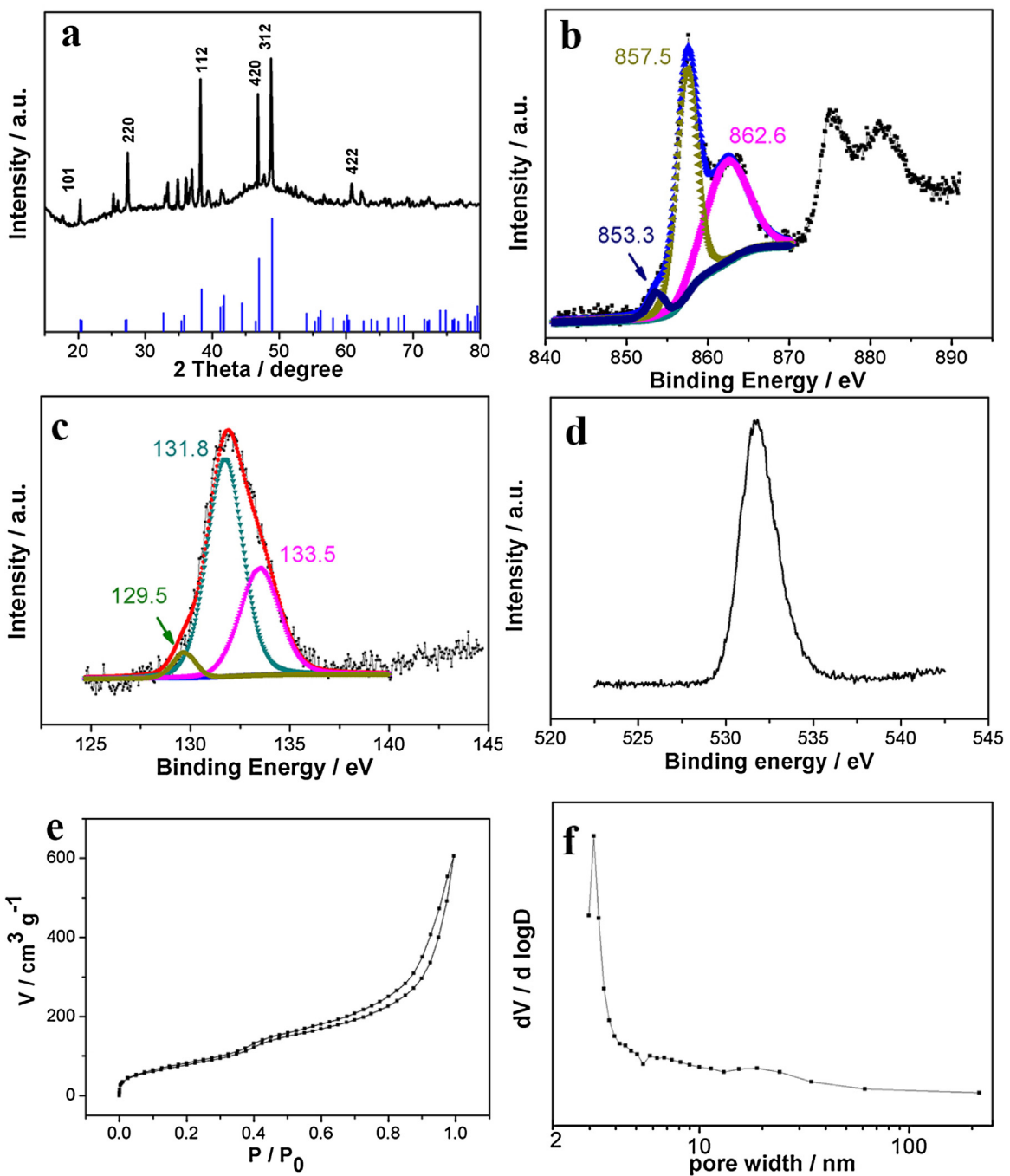


Fig. 1. XRD patterns (a); XPS spectra of Ni 2p 3/2(b), P 2p (c) and O 1s (d) windows; N_2 adsorption-desorption isotherms (e) and BJH pore-size distribution (f) of the $Ni_{12}P_5/Ni_3(PO_4)_2$ -HS.

first intercept of the main arc, all data have been corrected for 90% iR potential drop. EIS were recorded at the frequency range from 100 kHz to 0.1 Hz with 10 points per decade. The amplitude of the sinusoidal potential signal was 5 mV.

The generated gas was confirmed by gas chromatography analysis and measured quantitatively using a calibrated pressure sensor to monitor the pressure change in the anode compartment of a H-type electrolytic cell. The glass carbon sheet (1×2 cm) was used as working electrode with a catalysts loading of 0.71 mg cm^{-2} . The Faradaic efficiency was calculated by comparing the amount of measured oxygen with calculated oxygen generated at a constant oxidative current of 10 mA cm^{-2} in 1 M KOH for at least 80 min electrolysis (assuming 100% FE). Pressure data during electrolysis

were recorded using a CEM DT-8890 Differential Air Pressure Gauge Manometer Data Logger Meter Tester with a sampling interval of 1 point per second.

2.5. Fabrication of membrane electrode assembly (MEA) with catalyst-coated substrate (CCS) method

The MEA was prepared according to Reference [47]. $Ni_{12}P_5/Ni_3(PO_4)_2$ -HS was used as anode catalyst for oxygen evolution reaction (OER) and used as cathode catalysts for hydrogen evolution reaction (HER). The untreated carbon paper (TGPH#90, Toray Inc., Japan) and titanium (Ti) foam was employed as cathode and anode gas diffusion layer (GDL), respectively. A

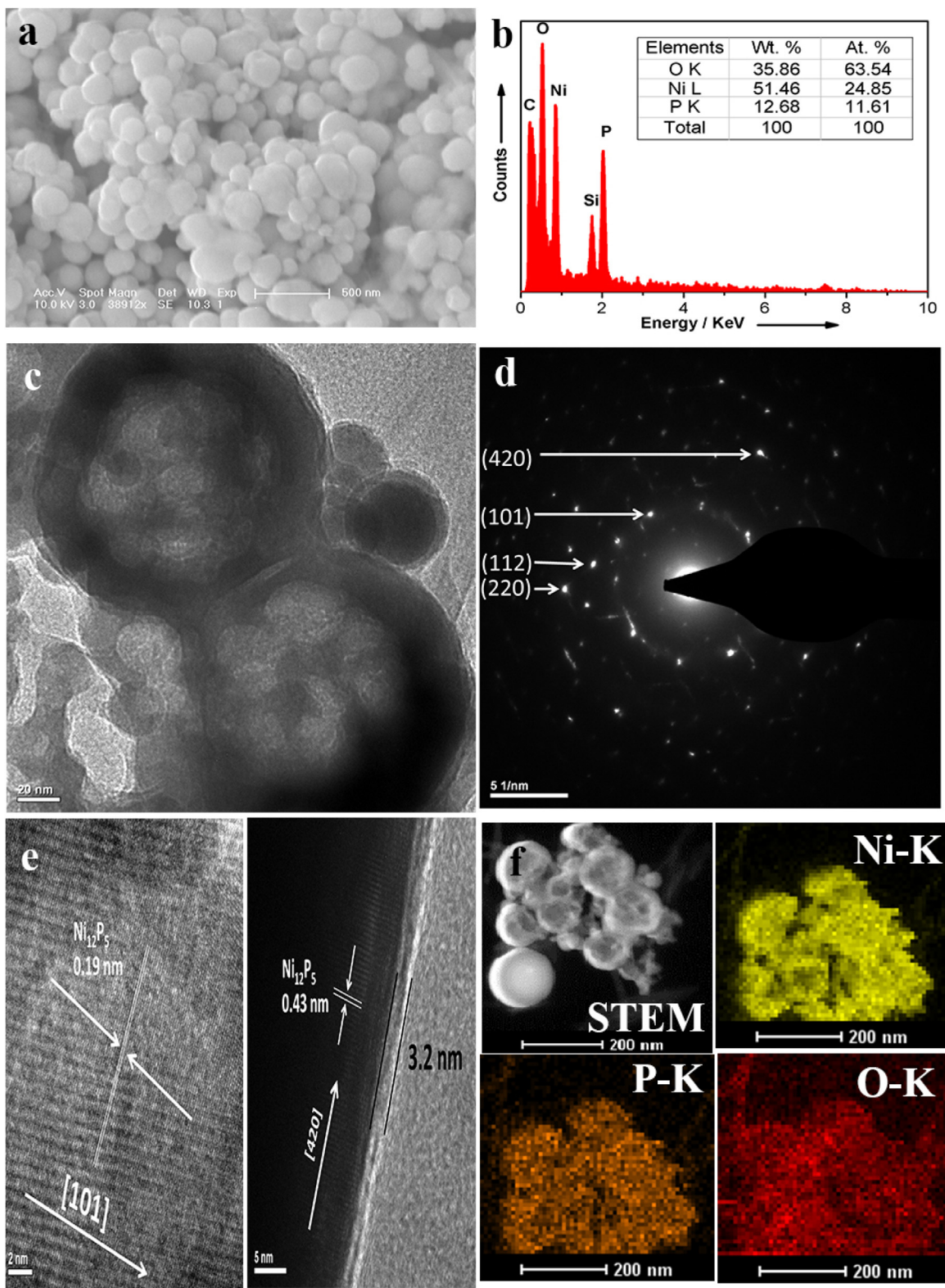


Fig. 2. SEM image (a) and obtained EDX spectrum (b), TEM image (c) and corresponding SAED image (d), HRTEM images (e) obtained from inside (left) and edge (right), STEM and elemental mapping (f) of the $\text{Ni}_{12}\text{P}_5/\text{Ni}_3(\text{PO}_4)_2$ —HS.

YAB membrane (Foma Corporation, Germany) with a thickness of 0.13–0.15 mm was used as anion exchange membrane (AEM). The catalysts were mixed with deionized water, isopropanol and PTFE ionomer suspension (10 wt% polymer in suspension) to obtain well dispersed ink using magnetic stirring combined with

ultrasonication. The as prepared ink was coated onto the surface of Ti foam and Toray TGP90 plain carbon paper using hand-pray method with the aid of a spray gun to obtain a CCS for the anode (oxygen evolution electrode) and the cathode (hydrogen evolution electrode) as well. The binder content (10 wt% PTFE ionomer) was

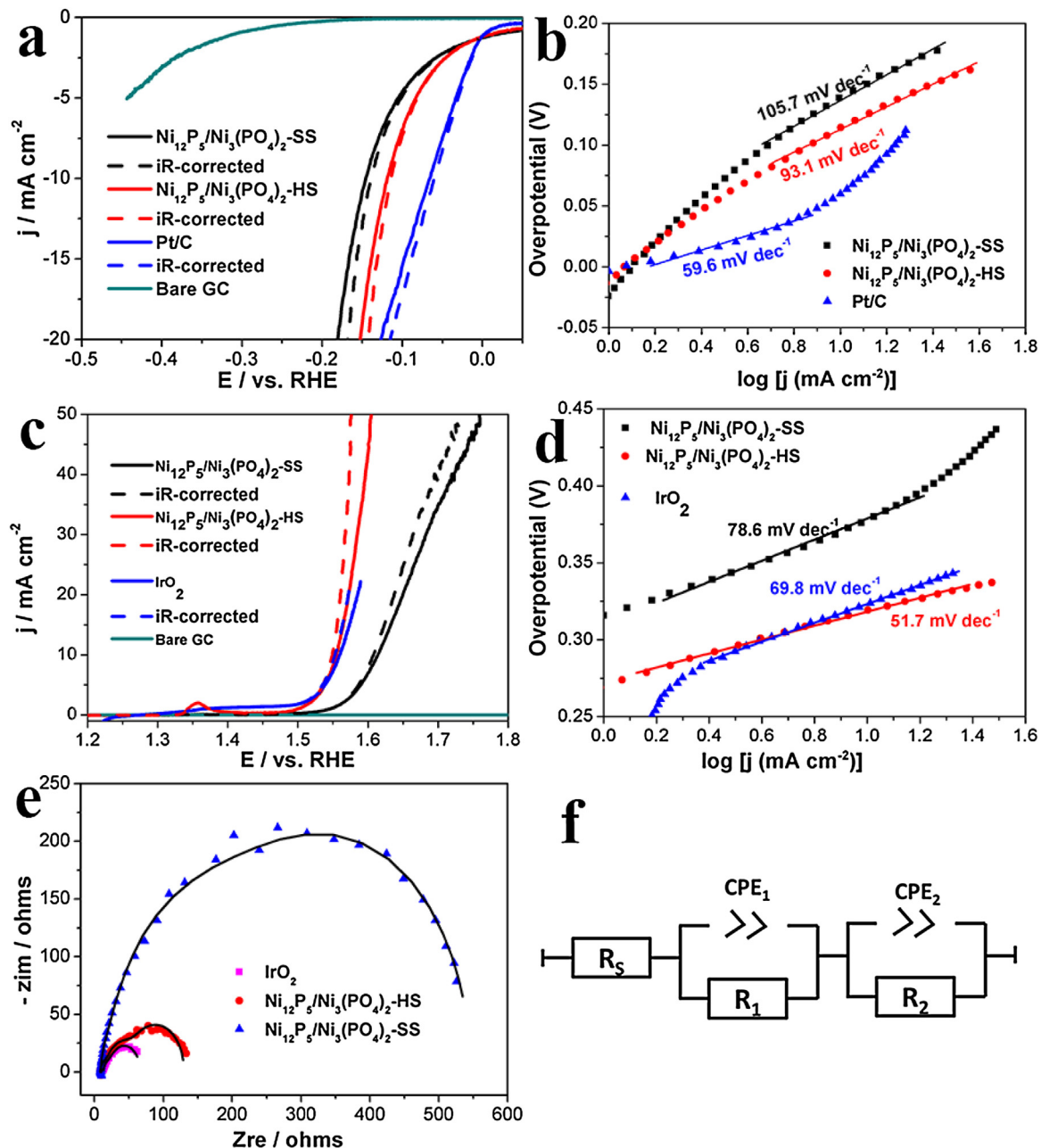


Fig. 3. Polarization curves (a) and Tafel slope (b) of $\text{Ni}_{12}\text{P}_5/\text{Ni}_3(\text{PO}_4)_2$ -SS, $\text{Ni}_{12}\text{P}_5/\text{Ni}_3(\text{PO}_4)_2$ -HS, commercial Pt/C and bare GC electrode for HER in nitrogen saturated 1 M KOH solutions; Polarization curves (c) and Tafel slope (d) of $\text{Ni}_{12}\text{P}_5/\text{Ni}_3(\text{PO}_4)_2$ -SS, $\text{Ni}_{12}\text{P}_5/\text{Ni}_3(\text{PO}_4)_2$ -HS, commercial IrO_2 and bare GC electrode for OER in oxygen saturated 1 M KOH solutions, scanning rate was 5 mV s^{-1} . Potentials were corrected with iR drop. Typical Nyquist plots (e) for OER catalyzed by a glassy carbon electrode with IrO_2 , $\text{Ni}_{12}\text{P}_5/\text{Ni}_3(\text{PO}_4)_2$ -HS and $\text{Ni}_{12}\text{P}_5/\text{Ni}_3(\text{PO}_4)_2$ -SS respectively at over-potential of 0.3 V; solid lines are the fitting. Electrical equivalent circuit (f) used to model the data from impedance measurements.

~5 wt% polymer for both anode and cathode catalysts layer. The loading of catalysts was both 3 mg/cm^2 for the anode and cathode catalysts layer, respectively. The catalyst-coated substrate was maintaining at 250°C for 1 h. The size of all electrode catalysts layer was $\pi \times 2 \text{ cm} \times 2 \text{ cm}$ (i.e. 12.56 cm^2 active areas). Anode CCS, YAB membrane and cathode CCS were assembled together in the cell hardware to form an MEA.

2.6. Cell performance evaluation

A ring-shaped water electrolysis setup (diameter, 4 cm) was used to evaluate the performance and durability of a single water electrolysis cell. Cell potential and current was controlled through

an Arbin testing system (Arbin Instruments, United States) and provided a direct electric current across the electrolysis cell to split the water and produce hydrogen at the cathode and oxygen at the anode. 1 M KOH was supplied into anode chamber at a flow rate of 5 mL min^{-1} with a peristaltic pump (BT100-2J, LongerPump Co. China). The cell temperature was maintained at 50°C . Before polarization measurements, the electrolysis cell was pretreated at 100 mA cm^{-2} for 4 h to activate the catalyst layer. The polarization curves (current density vs. cell voltage) were obtained using the Arbin testing system in galvanodynamic mode, i.e., the steady-state polarization curve was measured by recording the cell potential for 1 min from the circuit voltage under constant current density. For the durability tests, a constant current of 300 mA cm^{-2} was applied

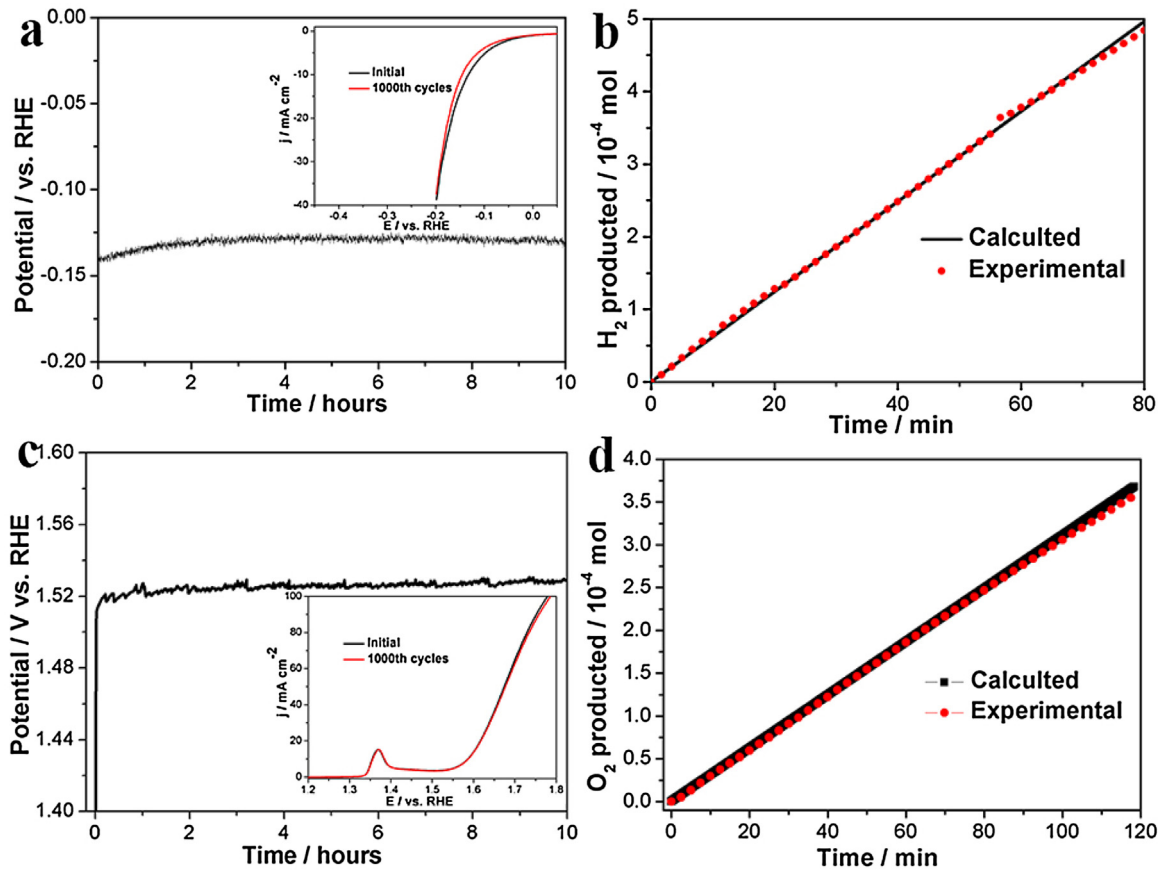


Fig. 4. Time-dependent potential curves for $\text{Ni}_{12}\text{P}_5/\text{Ni}_3(\text{PO}_4)_2\text{-HS}$ under a static current density of 10 mA cm^{-2} for 10 h for HER (a) and OER (c). Inset was polarization curves of initially and after 1000 CV scans with a scanning rate of 100 mV s^{-1} , the iR drop was not corrected. Calculated versus actual hydrogen (b) and oxygen (d) production catalyzed by $\text{Ni}_{12}\text{P}_5/\text{Ni}_3(\text{PO}_4)_2\text{-HS}$ at a constant oxidative current of 10 mA cm^{-2} in 1 M KOH .

onto the electrolysis cell, and the cell voltage as a function of test time was recorded by Arbin testing system. Before the durability tests, resistance was monitored by EIS. The EIS experiments were undertaken at a potential of 1.5 V vs. DHE (dynamic hydrogen electrode) using the same procedure as described elsewhere in our group earlier report. [48] The polarization curve was corrected with 90% iR drop.

3. Result and discussion

Fig. 1a shows the X-ray diffraction (XRD) pattern of the as-synthesized $\text{Ni}_{12}\text{P}_5/\text{Ni}_3(\text{PO}_4)_2\text{-HS}$. Peaks at $2\theta = 20.5, 27.4, 38.3, 46.9, 49$ and 60.8° are corresponding to $(101), (220), (112), (420), (312)$ and (422) planes of the Ni_{12}P_5 crystal, in sequence (JCPDS no. 65-1623). Besides the Ni_{12}P_5 peaks, other peaks with smaller relative intensities are observed, corresponding to the nickel phosphate $[\text{Ni}_3(\text{PO}_4)_2]$ phase. This result is consistent with the observation of Huang[43] and our previous work [44]. The chemical states of Ni and P in $\text{Ni}_{12}\text{P}_5/\text{Ni}_3(\text{PO}_4)_2\text{-HS}$ were investigated by high-resolution X-ray photoelectron spectroscopy (XPS), as shown in **Fig. 1b-d**, and the survey spectroscopy can be seen in Fig. S1. Three peaks at $853.3, 857.5$, and 862.6 eV are found in the XPS spectrum of the Ni 2p 3/2 window. The peak at 853.3 eV originates from Ni in phosphide, which is close to that of zero valence state Ni ($\text{Ni}^0, 852.8 \text{ eV}$). The positive shift in binding energy (0.5 eV) suggests that Ni has partly donates its electron to P to form an electron deficient state with positive charge ($\text{Ni}^{\delta+}, 0 < \delta < 1$). In the P 2p spectrum, three doublets at $129.5, 131.8$ and 133.5 eV were observed. The doublet at 129.5 eV corresponds to P in phosphide, where the

peak shifted negatively by 0.5 eV in comparison to elemental P (130.0 eV), suggesting the negatively charged ($\text{P}^{\delta-}, 0 < \delta < 1$) nature of P in phosphide. In addition, the peaks at 857.5 and 862.6 eV in the Ni 2p 3/2 spectrum and the doublet at 131.8 and 133.5 eV in the P 2p spectrum are likely be correlated with nickel phosphate formed on the surface of Ni_{12}P_5 , owing to the spontaneous passivation of sample exposed in air. [42,43,49] The surface ratio of P (0): P (V) was calculated from the deconvoluted areas, and the results show that PO_4^{3-} is the major component on the surface (Table S1), indicating the formation of $\text{Ni}_3(\text{PO}_4)_2$. The XPS of O shown in **Fig. 1d** further confirms the formation of nickel phosphate. The bulk composition of the catalysts was analyzed by ICP (Inductively Coupled Plasma-Optical Emission Spectroscopy), and the molar ratio of Ni: P was determined to be $2.45:1$, indicating the formation of Ni_{12}P_5 in bulk. Hence, combining the results from XRD, XPS, and ICP analysis, it is confirmed that the final product possesses a $\text{Ni}_3(\text{PO}_4)_2$ shell and Ni_{12}P_5 hollow core structure, which is proved by the TEM shown in following section. **Fig. 1e** shows the nitrogen adsorption/desorption isotherm of the $\text{Ni}_{12}\text{P}_5/\text{Ni}_3(\text{PO}_4)_2\text{-HS}$, and a type IV isotherm was observed, indicating the mesoporous nature of the catalyst. Ultrahigh Brunauer-Emmett-Teller (BET) specific surface area (SSA) at $289.2 \text{ m}^2 \text{ g}^{-1}$ was acquired, which is much larger than other reported Ni_{12}P_5 solid spheres [50]. The Barrett-Joyner-Halenda (BJH) pore size distribution curve (**Fig. 1f**) shows that the $\text{Ni}_{12}\text{P}_5/\text{Ni}_3(\text{PO}_4)_2\text{-HS}$ catalysts possess an average pore diameter of 3.1 nm . The counterpart $\text{Ni}_{12}\text{P}_5/\text{Ni}_3(\text{PO}_4)_2\text{-SS}$ catalyst was also characterized with XRD patterns shown in Fig. S2. Much smaller BET at $38.2 \text{ m}^2 \text{ g}^{-1}$ was acquired with average pore diameter located at 3.7 nm , as shown in Fig. S3.

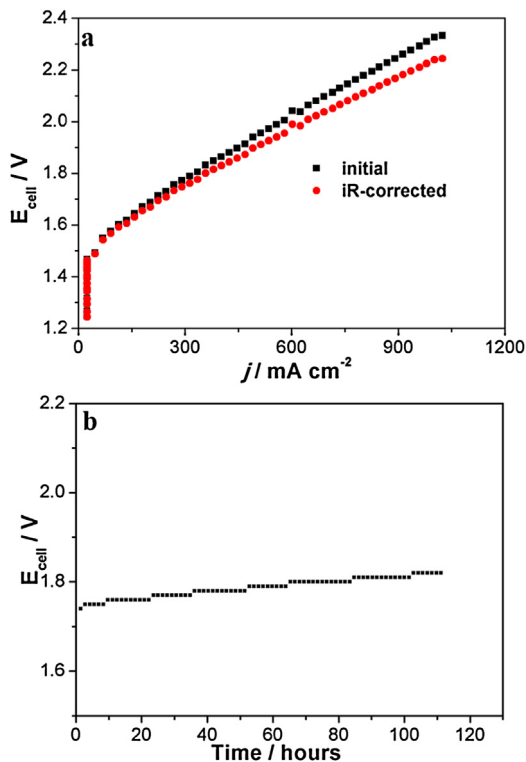


Fig. 5. Initial and after iR correction polarization curve (a) and cell voltage as a function of test time (b) at current density of 300 mA cm^{-2} for 110 h, the loading of $\text{Ni}_{12}\text{P}_5/\text{Ni}_3(\text{PO}_4)_2\text{-HS}$ catalyst for both side was 3 mg cm^{-2} ; Operation conditions: $T = 50^\circ\text{C}$ and 1 M KOH into the anode-feed with flow rate of 5 mL min^{-1} , both sides are under ambient pressure.

Fig. 2a–c depicts the scanning electron microscope (SEM), energy-dispersive X-ray spectrum (EDX), and transmission electron microscopy (TEM) images of the obtained $\text{Ni}_{12}\text{P}_5/\text{Ni}_3(\text{PO}_4)_2\text{-HS}$. Uniform spherical structure with diameters ranging from 150 to 250 nm and wall thickness of 20–40 nm was obtained. The corresponding EDX spectrum verifies that the $\text{Ni}_{12}\text{P}_5/\text{Ni}_3(\text{PO}_4)_2\text{-HS}$ consists exclusively of Ni, P and O (C and Si was come from matrix). No peaks from other elements were observed, which was in consistent with XPS and ICP characterization. The HAADF-STEM (High-angle annular dark-field scanning TEM) image and the corresponding elemental maps (**Fig. 2f**) confirm the uniform distribution of Ni, P, and O over the whole Ni_{12}P_5 hollow sphere without segregation. Selected-area electron diffraction (SAED, **Fig. 2d**) shows the catalyst displays a well-defined spotted pattern corresponding to the diffraction along the (101), (112), (220) and (420) planes of a tetragonal Ni_{12}P_5 structure. **Fig. 2e** shows HR-TEM images of the $\text{Ni}_{12}\text{P}_5/\text{Ni}_3(\text{PO}_4)_2\text{-HS}$ in the bulk and at the outside edge of the catalyst, where highly ordered crystalline structure is observed. The interplanar spacing noticed at 0.19 nm and 0.43 nm correspond to the (101) and (420) facets of Ni_{12}P_5 , respectively. Furthermore, the core-shell structure is clearly noticed with Ni_{12}P_5 crystalline coated by a thin amorphous layer (3.2 nm). The shell, formed from reaction with oxygen, is confirmed as $\text{Ni}_3(\text{PO}_4)_2$ by above XRD and XPS characterization. Thus, the end-product was $\text{Ni}_{12}\text{P}_5/\text{Ni}_3(\text{PO}_4)_2\text{-HS}$ with Ni_{12}P_5 hollow spheres coated by a thin $\text{Ni}_3(\text{PO}_4)_2$ shell. The SEM and TEM images of $\text{Ni}_{12}\text{P}_5/\text{Ni}_3(\text{PO}_4)_2\text{-SS}$ are shown in **Fig. S4**, particle diameters of 150–250 nm are noticed (same to $\text{Ni}_{12}\text{P}_5/\text{Ni}_3(\text{PO}_4)_2\text{-HS}$), thus making the particle size effect irrelevant during the discussion of catalytic performance.

The catalytic activity towards the HER of $\text{Ni}_{12}\text{P}_5/\text{Ni}_3(\text{PO}_4)_2\text{-HS}$ was first evaluated by negative potential sweeping (from 0.1 to -0.2 V versus RHE) in a three-electrode setup. The performance

of Pt/C and bare glass carbon electrode (GCE) were also tested for comparison. As shown in **Fig. 3a**, it is evident that bare GCE possesses no HER catalytic activity before -0.3 V . In contrast, a rapid cathodic current rise was observed for all other three catalysts modified electrodes. The over potentials for $\text{Ni}_{12}\text{P}_5/\text{Ni}_3(\text{PO}_4)_2\text{-SS}$, $\text{Ni}_{12}\text{P}_5/\text{Ni}_3(\text{PO}_4)_2\text{-HS}$, and Pt/C to reach current density at 10 mA cm^{-2} are 0.145, 0.114, and 0.065 V, respectively. A steeper current curve is noticed on the $\text{Ni}_{12}\text{P}_5/\text{Ni}_3(\text{PO}_4)_2\text{-HS}$ in comparison to Pt/C, thus leading to even closer over potential for the two catalysts at higher current densities. For instance, at 20 mA cm^{-2} , the over potential on $\text{Ni}_{12}\text{P}_5/\text{Ni}_3(\text{PO}_4)_2\text{-HS}$ (0.142 V) is only 26 mV higher than that on the Pt/C (0.116 V), much better than most reported non-precious metal catalysts [23] as list in Table S2. It is well known that the HER generally involves three possible reaction steps in acidic media, while the HER mechanism in alkaline media is still ambiguous [9]. However, it is clear that the smaller the Tafel values is, the faster and easier of hydrogen generation in alkaline media. The Tafel slopes (**Fig. 3b**) for $\text{Ni}_{12}\text{P}_5/\text{Ni}_3(\text{PO}_4)_2\text{-SS}$, $\text{Ni}_{12}\text{P}_5/\text{Ni}_3(\text{PO}_4)_2\text{-HS}$, and Pt/C were 105.7, 93.1 and 59.6 mV dec^{-1} , respectively, which indicate that $\text{Ni}_{12}\text{P}_5/\text{Ni}_3(\text{PO}_4)_2\text{-HS}$ possesses a much faster HER kinetics rate than $\text{Ni}_{12}\text{P}_5/\text{Ni}_3(\text{PO}_4)_2\text{-SS}$. Catalytic OER activity was examined through CV measurements in O_2 -saturated 1 M KOH aqueous solution at a scan rate of 5 mV s^{-1} . The representative iR-corrected LSV and Tafel plots are shown in **Fig. 3c** and d. The oxidation peaks located in 1.326 to 1.407 V vs RHE for Ni-based catalysts are ascribed to Ni^{2+} to Ni^{3+} , which have been observed in most of Ni-based electrocatalysts [31,51,52]. Excitingly, the $\text{Ni}_{12}\text{P}_5/\text{Ni}_3(\text{PO}_4)_2\text{-HS}$ catalyst shows advanced catalytic activity for OER, i.e., manifesting low over potential at 0.318, 0.331 and 0.368 V to reach current densities at 10, 20 and 50 mA cm^{-2} , in sequence, which is even better than the state-of-the-art commercial IrO_2 catalysts. The $\text{Ni}_{12}\text{P}_5/\text{Ni}_3(\text{PO}_4)_2\text{-SS}$ catalyst shows much inferior performance, and over potentials of 0.378, 0.407 and 0.498 V were required to reach current density at 10, 20 and 50 mA cm^{-2} , respectively. In addition, the $\text{Ni}_{12}\text{P}_5/\text{Ni}_3(\text{PO}_4)_2\text{-HS}$ electrode shows the smallest Tafel slope value (51.7 mV dec^{-1}) amongst all the samples investigated, corresponding to the most favorable OER kinetics (See Table S3).

To study the electrode kinetics as well as the solution resistance (R_S), **Fig. S5** shows Nyquist plots of the impedance data at different over-potentials for HER and OER catalyzed by different catalysts. Typical Nyquist plots for OER at over-potential of 0.3 V was shown in **Fig. 3e** (**Fig. S6** is the high frequencies area drive from **Fig. 3e**) and the equivalent circuit was shown in **Fig. 3f**. Here, the resistance element R_S corresponds to the uncompensated solution resistance, while R_1 corresponds to charge transfer resistance arisen from OER, CPE_1 (constant-phase element) is the double layer capacitance, the second time constant (R_2 and CPE_2) is probably related to the contact between the glassy carbon electrode and the catalyst [41]. The data calculated from the equivalent circuit are compared in Table S4. The R_S for IrO_2 , $\text{Ni}_{12}\text{P}_5/\text{Ni}_3(\text{PO}_4)_2\text{-HS}$ and $\text{Ni}_{12}\text{P}_5/\text{Ni}_3(\text{PO}_4)_2\text{-SS}$ is 9.844, 8.684 and 9.228Ω , respectively; these values are used to compensated solution resistance. Furthermore, the charge transfer resistance of $\text{Ni}_{12}\text{P}_5/\text{Ni}_3(\text{PO}_4)_2\text{-HS}$ is only 36.84Ω , much smaller than $\text{Ni}_{12}\text{P}_5/\text{Ni}_3(\text{PO}_4)_2\text{-SS}$ (327.2Ω), indicated the $\text{Ni}_{12}\text{P}_5/\text{Ni}_3(\text{PO}_4)_2\text{-HS}$ possess much faster electrode reaction kinetics than $\text{Ni}_{12}\text{P}_5/\text{Ni}_3(\text{PO}_4)_2\text{-SS}$. Furthermore, the BET of $\text{Ni}_{12}\text{P}_5/\text{Ni}_3(\text{PO}_4)_2\text{-HS}$ ($289.2 \text{ m}^2 \text{ g}^{-1}$) is much bigger than $\text{Ni}_{12}\text{P}_5/\text{Ni}_3(\text{PO}_4)_2\text{-SS}$ ($38.2 \text{ m}^2 \text{ g}^{-1}$), the bigger BET will provide much more active sites, as well as benefit for the sufficient contact between active sites and reactants. Hence, the $\text{Ni}_{12}\text{P}_5/\text{Ni}_3(\text{PO}_4)_2\text{-HS}$ possess much better performance than $\text{Ni}_{12}\text{P}_5/\text{Ni}_3(\text{PO}_4)_2\text{-SS}$.

The durability of the $\text{Ni}_{12}\text{P}_5/\text{Ni}_3(\text{PO}_4)_2\text{-HS}$ catalyst was investigated through a 24 h galvanostatic measurement (**Fig. 4a** and c) at 10 mA cm^{-2} and continuous cyclic voltammetric (CV) sweeps for 1000 cycles (inset in **Fig. 4a** and c). As seen, the $\text{Ni}_{12}\text{P}_5/\text{Ni}_3(\text{PO}_4)_2\text{-HS}$

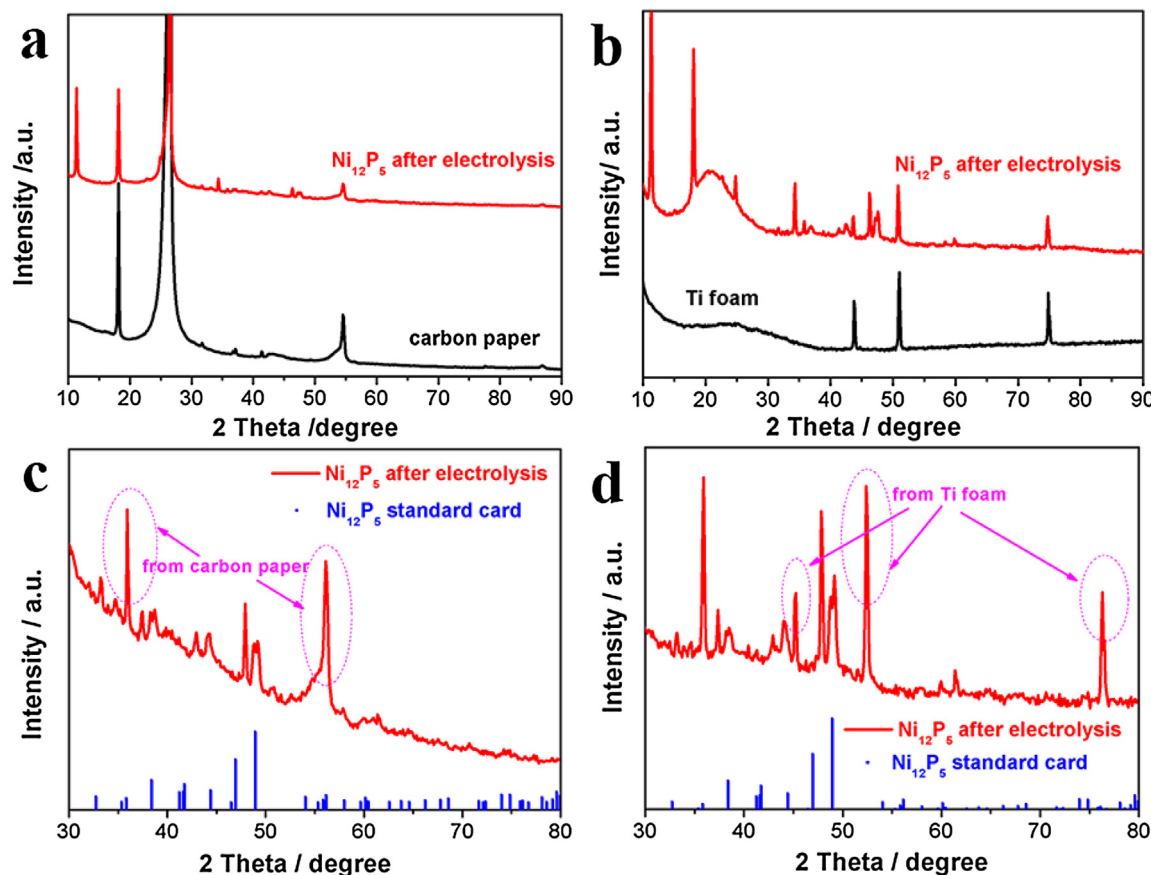


Fig. 6. XRD patterns of $\text{Ni}_{12}\text{P}_5/\text{Ni}_3(\text{PO}_4)_2$ -HS after electrolysis on cathode HER side (a and c) and anode OER side (b and d).

HS is stable over long-term testing both for HER and OER. The slight decay observed in the initial 2 min originates from the physical adsorption of the generated H_2/O_2 bubbles on the electrode surface, which caused the reduction in active surface area [53]. The Faradaic efficiency (FE) of the electrocatalytic hydrogen/oxygen evolution process (Fig. S7 shows optical photograph about the generation of hydrogen/oxygen bubbles during the $\text{Ni}_{12}\text{P}_5/\text{Ni}_3(\text{PO}_4)_2$ -HS FE test) were analyzed by comparing the amount of experimentally quantified hydrogen/oxygen with the theoretically calculated hydrogen/oxygen. As shown in Fig. 4b and d, the perfectly match of the two plots for the $\text{Ni}_{12}\text{P}_5/\text{Ni}_3(\text{PO}_4)_2$ -HS catalyst indicates a current efficiency at 100%.

The $\text{Ni}_{12}\text{P}_5/\text{Ni}_3(\text{PO}_4)_2$ -HS was adopted as both anode and cathode catalysts in a real electrolyzer with anion exchange membrane (AEM) acting as the solid electrolyte. The polarization curves are shown in Fig. 5a, a current density of 357.6 mA cm^{-2} was acquired at 1.8 V after iR correction (Fig. S8 shows the Nyquist plots at 1.5 V), which is rather competitive to the cell using IrO_2 anode and Pt black cathode (399 mA cm^{-2} at 1.8 V) in same testing condition at much lower cost [47,54]. Moreover, with further optimization in cell structure, which is now optimized for Pt/IrO_2 based catalysts, even higher performance is expected for the $\text{Ni}_{12}\text{P}_5/\text{Ni}_3(\text{PO}_4)_2$ -HS. Fig. 5b shows the constant current test of the electrolysis cell with current density held at 300 mA cm^{-2} , the cell voltage was found increased only by 70 mV after 110 h , which indicates the $\text{Ni}_{12}\text{P}_5/\text{Ni}_3(\text{PO}_4)_2$ -HS as a promising candidate for future water electrolysis.

To further investigate the origin of cell degradation, both anode and cathode catalysts were subjected to physical characterization including XRD, SEM, TEM and XPS after operating at 300 mA cm^{-2} for 110 h . Fig. 6a-d are the (enlarged) XRD patterns

of the $\text{Ni}_{12}\text{P}_5/\text{Ni}_3(\text{PO}_4)_2$ -HS after cell operation. No distinguishable change in either anode or cathode crystalline structure was noticed after electrolysis, indicating an ultrahigh stability of the catalyst. Fig. 7 shows SEM and TEM images of both anode and cathode, where the structure was found well maintained after electrolysis. All the XRD, SEM and TEM characterizations indicate that $\text{Ni}_{12}\text{P}_5/\text{Ni}_3(\text{PO}_4)_2$ -HS well maintains its crystal structure and morphology in spite of the strong basic solutions (1 M KOH) and high current application over a long period (300 mA cm^{-2} with about 110 h).

Furthermore, XPS was also used to probe the surface structure evolution due to electrolysis, as shown in Fig. 8 and Table S1. After electrolysis on anode OER side, the peak position of $\text{Ni} 2\text{p}$ shifted positively, while the $\text{P} 2\text{p}$ peak shifted negatively, indicating the positive charge of Ni and negative charge of P , which may due to the occurrence of surface electron reorganization during the OER electrolysis. For the HER side, the binding energy of Ni and P are hardly changed compared to the freshly prepared $\text{Ni}_{12}\text{P}_5/\text{Ni}_3(\text{PO}_4)_2$ -HS, indicating $\text{Ni}_{12}\text{P}_5/\text{Ni}_3(\text{PO}_4)_2$ -HS is highly robust and stable when acting as a HER catalyst. The binding energy of $\text{O} 1\text{s}$ exhibit negligible changes for both HER and OER side (Fig. S9), which may be due to the exposure of the sample to air and soaking in KOH solution [43]. Hence, it is convincing that the performance loss of AEMWE mainly resulted from degradation at the OER side, the much higher over potential used in anode OER side results in surface electrons reorganization, thus leading to faster cell performance degradation. In addition, we also tested the internal resistance of electrolysis cell before and after electrolysis, and the value was 0.148Ω and 0.347Ω , respectively. Hence, the deterioration in interfacial contact and membrane degradation are other important factors for the performance loss.

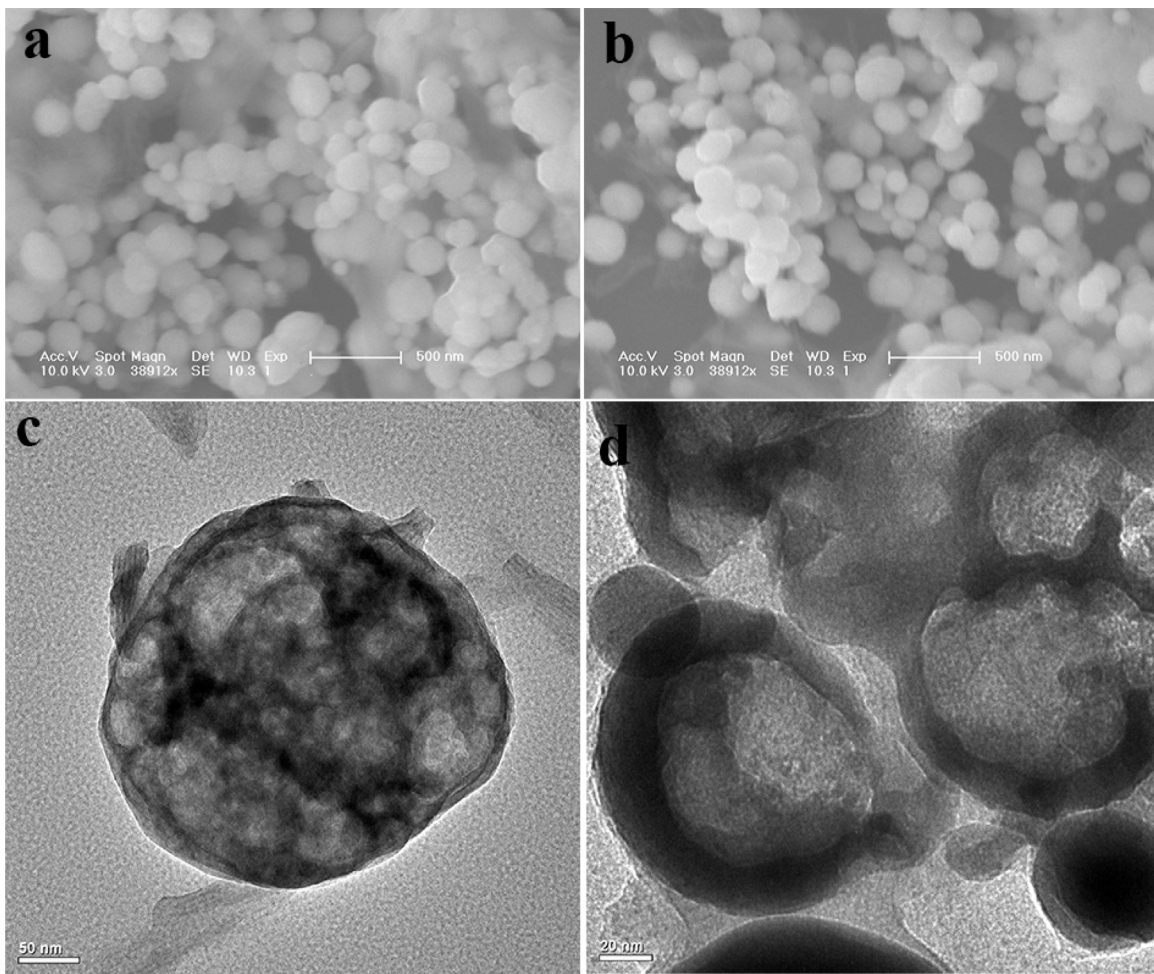


Fig. 7. SEM and TEM images of $\text{Ni}_{12}\text{P}_5/\text{Ni}_3(\text{PO}_4)_2$ -HS after electrolysis on anode OER side (a and c) and cathode HER side (b and d).

It was reported that Ni_{12}P_5 is an effective HER catalyst [43,49,50] while CoPi can act as an effective OER catalyst [55]. Based on this point, we prepared bulk $\text{Ni}_3(\text{PO}_4)_2$ with the BET of $31.61 \text{ m}^2 \text{ g}^{-1}$ and average pore diameter of 3.7 nm , and the results are shown in Fig. S10. The catalytic activities of bulk $\text{Ni}_3(\text{PO}_4)_2$ for OER and HER were shown in Fig. S11, where considerable OER activity was observed on bulk $\text{Ni}_3(\text{PO}_4)_2$ itself. The bulk $\text{Ni}_3(\text{PO}_4)_2$ electrode reached 10 mA cm^{-2} at over-potential of 0.42 V and possessed a Tafel slope of 116 mV dec^{-1} (Fig. S11a). What's more, after 1000 cycles accelerated stability tests (Fig. S11b), hardly any performance decay was observed.

To further investigate the quantitative relationship and provide further insight into the catalytic processes, the specific activities (normalized to BET specific surface area, SSA) for OER is studied. As shown in Fig. 3c, the OER activities at 1.6 V before normalization are 8.3 , 98.1 and 3.8 mA cm^{-2} for $\text{Ni}_{12}\text{P}_5/\text{Ni}_3(\text{PO}_4)_2$ -SS, $\text{Ni}_{12}\text{P}_5/\text{Ni}_3(\text{PO}_4)_2$ -HS and bulk $\text{Ni}_3(\text{PO}_4)_2$ in sequence, where the activity of $\text{Ni}_{12}\text{P}_5/\text{Ni}_3(\text{PO}_4)_2$ -HS is more than one magnitude higher (12-fold and 26-fold in comparison to $\text{Ni}_{12}\text{P}_5/\text{Ni}_3(\text{PO}_4)_2$ -SS and $\text{Ni}_3(\text{PO}_4)_2$) than the $\text{Ni}_{12}\text{P}_5/\text{Ni}_3(\text{PO}_4)_2$ -SS and $\text{Ni}_3(\text{PO}_4)_2$. After normalization (Fig. S12a), however, the differences become much smaller, and the specific activities are calculated as 0.0288 ($\text{Ni}_{12}\text{P}_5/\text{Ni}_3(\text{PO}_4)_2$ -SS), 0.0473 ($\text{Ni}_{12}\text{P}_5/\text{Ni}_3(\text{PO}_4)_2$ -HS) and $0.0167 \text{ mA cm}^{-2}$ ($\text{Ni}_3(\text{PO}_4)_2$), respectively. Comparing the two sets of results, it is obvious that the high specific surface area of $\text{Ni}_{12}\text{P}_5/\text{Ni}_3(\text{PO}_4)_2$ -HS is the main reason for its super activity. As for the differences in SSA normalized catalytic activity, the variation in electric conductivity may play a significant role, where

the influence of electrical conductivity on the catalytic performance was proved for long [56]. Hence, a typical four-probe method was used to probe and compare the electrical resistance of $\text{Ni}_{12}\text{P}_5/\text{Ni}_3(\text{PO}_4)_2$ -HS, $\text{Ni}_{12}\text{P}_5/\text{Ni}_3(\text{PO}_4)_2$ -SS and bulk $\text{Ni}_3(\text{PO}_4)_2$. The conductivity of $\text{Ni}_{12}\text{P}_5/\text{Ni}_3(\text{PO}_4)_2$ -HS and $\text{Ni}_{12}\text{P}_5/\text{Ni}_3(\text{PO}_4)_2$ -SS was 2.79 and 2.55 S/cm , while a much lower value of 0.165 S/cm was observed for bulk $\text{Ni}_3(\text{PO}_4)_2$. Therefore, the lower performance of $\text{Ni}_3(\text{PO}_4)_2$ is suspected to be caused by its lower conductivity, which increases the charge transfer resistance during the reaction. To verify this hypothesis, we used active carbon (Vulcan XC-72, denoted as C) to compensate the lower conductivity of bulk $\text{Ni}_3(\text{PO}_4)_2$ by mixing with C (mass ratio, 1:1), the mixture is denoted as $\text{Ni}_3(\text{PO}_4)_2/\text{C}$. The performance of $\text{Ni}_3(\text{PO}_4)_2/\text{C}$ for OER can be seen in Fig. S13, and the performance of $\text{Ni}_3(\text{PO}_4)_2/\text{C}$ with and without active carbon can be seen in Fig. S14. From Fig. S14, it is clearly observed that after mixing with active carbon, the OER performance improved obviously. For example, to reach a current density of 10 mA cm^{-2} , the bulk $\text{Ni}_3(\text{PO}_4)_2$ need an over-potential of 420 mV , while it only need 337 mV over-potential for $\text{Ni}_3(\text{PO}_4)_2/\text{C}$. In addition, the Tafel slope of bulk $\text{Ni}_3(\text{PO}_4)_2$ and $\text{Ni}_3(\text{PO}_4)_2/\text{C}$ for OER is 116 and 91.9 mV dec^{-1} respectively. These indicate that the intrinsic activity of $\text{Ni}_3(\text{PO}_4)_2$ for OER is admirable, but the activity is limited by its low conductivity. Therefore, with higher conductivity of Ni_{12}P_5 in the core, higher SSA normalized catalytic performance of $\text{Ni}_{12}\text{P}_5/\text{Ni}_3(\text{PO}_4)_2$ catalysts were obtained. The slight difference in SSA normalized activity between the hollow spheres and the solid spheres can be ascribed to the slight difference in the electrode

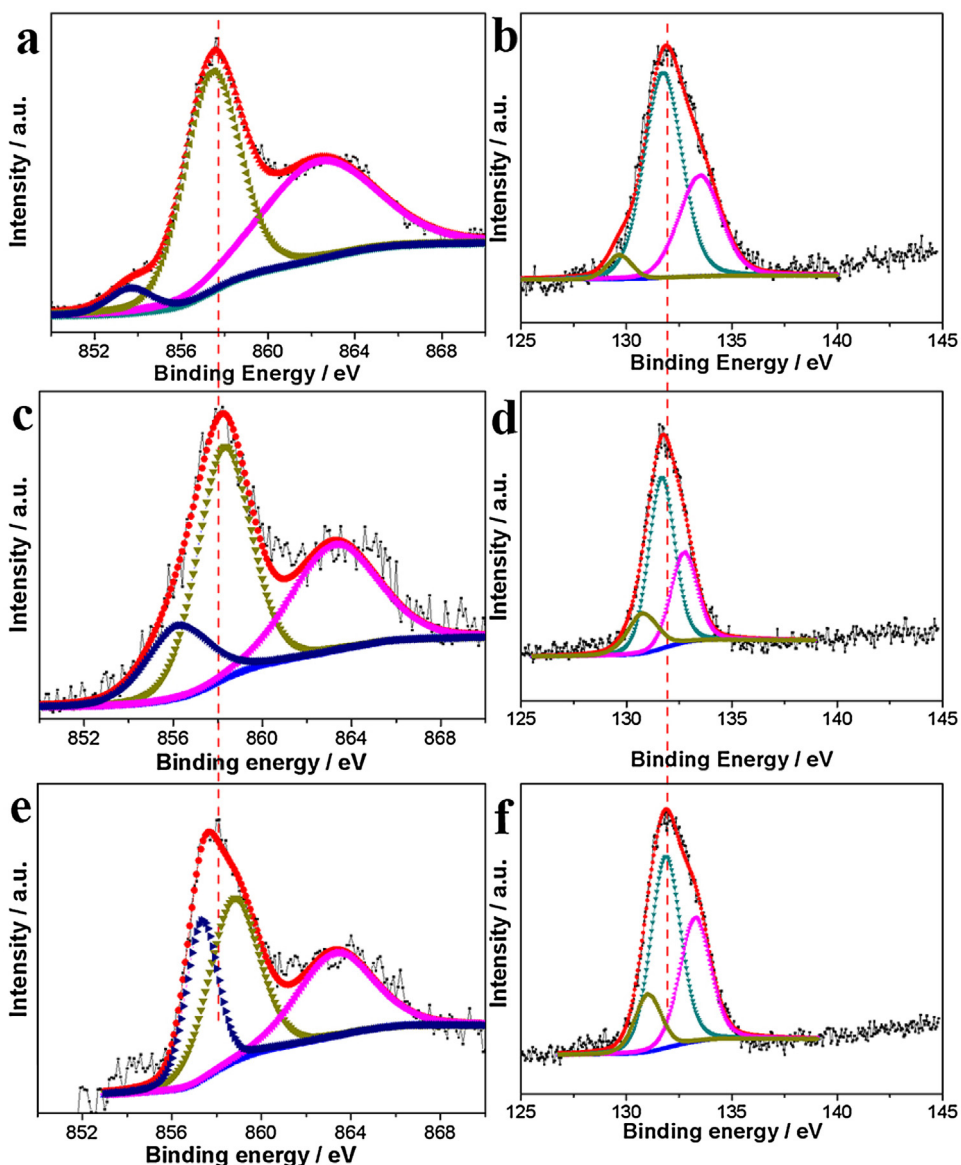


Fig. 8. Comparison the high-resolution XPS patterns for Ni 2p (a, c and e) and P 2p (b, d and f) of the fresh prepared $\text{Ni}_{12}\text{P}_5/\text{Ni}_3(\text{PO}_4)_2$ -HS (a and b) with the $\text{Ni}_{12}\text{P}_5/\text{Ni}_3(\text{PO}_4)_2$ -HS that after electrolysis on anode OER side (c and d) and cathode HER side (e and f).

microstructure, such as the difference in shell and core thickness, etc.

The HER performance of bulk $\text{Ni}_3(\text{PO}_4)_2$ is shown in Fig. S11c and S11d, the electrode does not show any appreciable cathodic current for H_2 evolution in the potential range of -0.4 – 0 V vs. RHE. The bulk $\text{Ni}_3(\text{PO}_4)_2$ electrode reached 10 mA cm^{-2} at over-potential of 0.484 V and possessed a Tafel slope of $114.8 \text{ mV dec}^{-1}$. The much slower HER process and the higher Tafel slope indicates negligible contribution of $\text{Ni}_3(\text{PO}_4)_2$ on the $\text{Ni}_{12}\text{P}_5/\text{Ni}_3(\text{PO}_4)_2$ -HS for HER and precludes the possibility of $\text{Ni}_3(\text{PO}_4)_2$ being the active sites, where the activity for the three catalysts before normalization Fig. 3a at -0.1 V is 4.8 , 7.3 and 0.4 mA cm^{-2} , respectively, for $\text{Ni}_{12}\text{P}_5/\text{Ni}_3(\text{PO}_4)_2$ -SS, $\text{Ni}_{12}\text{P}_5/\text{Ni}_3(\text{PO}_4)_2$ -HS and bulk $\text{Ni}_3(\text{PO}_4)_2$. Nickel phosphide, on the other hand, has long been confirmed as the active sites and is also held as the active catalytic substance in this work. Therefore, the HER catalytic activity is not only related with the surface area of the catalysts, but strongly associated with the surface content of nickel phosphide, where the value was found to be $<5\%$ for $\text{Ni}_{12}\text{P}_5/\text{Ni}_3(\text{PO}_4)_2$ -HS. As a result (Fig. S12b), the normalized specific activity (SSA) of

$\text{Ni}_{12}\text{P}_5/\text{Ni}_3(\text{PO}_4)_2$ -HS ($0.00078 \text{ mA cm}^{-2}$) was found lower than that of $\text{Ni}_{12}\text{P}_5/\text{Ni}_3(\text{PO}_4)_2$ -SS ($0.0036 \text{ mA cm}^{-2}$), probably due to the higher exposed ratio of nickel phosphide in the latter catalysts. Hence, the $\text{Ni}_{12}\text{P}_5/\text{Ni}_3(\text{PO}_4)_2$ -HS can act as a difunctional and stable catalysts both for HER and OER in strong basic solutions.

4. Conclusions

In summary, a novel $\text{Ni}_{12}\text{P}_5/\text{Ni}_3(\text{PO}_4)_2$ -HS was prepared and found to be an effective and robust catalyst material for overall water splitting. The Ni_{12}P_5 hollow spheres as a core is active for HER and surface passivation $\text{Ni}_3(\text{PO}_4)_2$ shell is responsible for the superior performance for OER. The HER and OER activity for $\text{Ni}_{12}\text{P}_5/\text{Ni}_3(\text{PO}_4)_2$ -HS is superior to most state-of-the-art catalysts, where reaching 10 mA cm^{-2} only needs an over-potential of 0.318 V and 0.114 V for OER and HER, respectively. Furthermore, the current density was 357.6 mA cm^{-2} at 1.8 V when integrated into a practical AEMWE using $\text{Ni}_{12}\text{P}_5/\text{Ni}_3(\text{PO}_4)_2$ -HS both for anode and cathode catalyst, which is rather competitive to the state-of-the-art Pt/IrO_2 catalyst at much lower cost. These findings highlight the potential

of $\text{Ni}_{12}\text{P}_5/\text{Ni}_3(\text{PO}_4)_2$ -HS as a difunctional catalyst for future electrochemical water splitting devices and can simplify the structure thus promote mass production in energy devices.

Acknowledgements

The work is supported by the National Natural Science Foundation of China (21373199, 21433003), the Strategic Priority Research Program of CAS (XDA09030104), Jilin Province Science and Technology Development Program (20150101066JC, 20160622037JC) and the Recruitment Program of Foreign Experts (WQ20122200077), Prof. J. Ge thanks for the Hundred Talents Program of Chinese Academy of Science.

Appendix A. Supplementary data

Supplementary data associated with this article can be found, in the online version, at <http://dx.doi.org/10.1016/j.apcatb.2016.11.050>.

References

- [1] M.D. Karkas, O. Verho, E.V. Johnston, B. Åkermark, *Chem. Rev.* 114 (2014) 11863–12001.
- [2] M.G. Walter, E.L. Warren, J.R. McKone, S.W. Boettcher, E.A.S. Qixi Mi, N.S. Lewis, *Chem. Rev.* 110 (2010) 6446–6473.
- [3] A.L. Goff, V. Artero, B. Josselme, P.D. Tran, N. Guillet, R. Métayé, A. Fihri, S. Palacin, M. Fontecave, *Science* 326 (2009) 1384–1387.
- [4] J. Deng, P. Ren, D. Deng, L. Yu, F. Yang, X. Bao, *Energy Environ. Sci.* 7 (2014) 1919–1923.
- [5] S.D. Ebbesen, S.H. Jensen, A. Hauch, M.B. Mogensen, *Chem. Rev.* 114 (2014) 10697–10734.
- [6] J. Chang, Y. Xiao, Z. Luo, J. Ge, C. Liu, W. Xing, *Acta Phys.–Chim. Sin.* 32 (2016) 1556–1592.
- [7] S. Hu, G. Goenaga, C. Melton, T.A. Zawodzinski, D. Mukherjee, *Appl. Catal. B: Environ.* 182 (2016) 286–296.
- [8] S. Siracusano, N. Van Dijk, E. Payne-Johnson, V. Baglio, A.S. Aricò, *Appl. Catal. B: Environ.* 164 (2015) 488–495.
- [9] X. Zou, Y. Zhang, *Chem. Soc. Rev.* 44 (2015) 5148–5180.
- [10] Y. Cheng, C. Xu, L. Jia, J.D. Gale, L. Zhang, C. Liu, P.K. Shen, S.P. Jiang, *Appl. Catal. B: Environ.* 163 (2015) 96–104.
- [11] S.H. Ahn, B.-S. Lee, I. Choi, S.J. Yoo, H.-J. Kim, E. Cho, D. Henkensmeier, S.W. Nam, S.-K. Kim, J.H. Jang, *Appl. Catal. B: Environ.* 154–155 (2014) 197–205.
- [12] E.J. Popczun, J.R. McKone, C.G. Read, A.J. Biacchi, A.M. Wiltrot, N.S. Lewis, R.E. Schaak, *J. Am. Chem. Soc.* 135 (2013) 9267–9270.
- [13] T.-W. Lin, C.-J. Liu, C.-S. Dai, *Appl. Catal. B: Environ.* 154–155 (2014) 213–220.
- [14] T.-W. Lin, C.-J. Liu, J.-Y. Lin, *Appl. Catal. B: Environ.* 134–135 (2013) 75–82.
- [15] Z. Wu, B. Fang, A. Bonakdarpour, A. Sun, D.P. Wilkinson, D. Wang, *Appl. Catal. B: Environ.* 125 (2012) 59–66.
- [16] X. Yu, R. Du, B. Li, Y. Zhang, H. Liu, J. Qu, X. An, *Appl. Catal. B: Environ.* 182 (2016) 504–512.
- [17] D. Kong, H. Wang, Z. Lu, Y. Cui, *J. Am. Chem. Soc.* 136 (2014) 4897–4900.
- [18] C. Tang, N. Cheng, Z. Pu, W. Xing, X. Sun, *Angew. Chem. Int. Ed.* 127 (2015) 9483–9487.
- [19] W. Cui, Q. Liu, Z. Xing, A.M. Asiri, K.A. Alamry, X. Sun, *Appl. Catal. B: Environ.* 164 (2015) 144–150.
- [20] F.H. Saadi, A.I. Carim, E. Verlage, J.C. Hemminger, N.S. Lewis, M.P. Soriaga, *J. Phys. Chem. C* 118 (2014) 29294–29300.
- [21] Z. Huang, Z. Chen, Z. Chen, C. Lv, M.G. Humphrey, C. Zhang, *Nano Energy* 9 (2014) 373–382.
- [22] D.V. Esposito, S.T. Hunt, Y.C. Kimmel, J.G. Chen, *J. Am. Chem. Soc.* 134 (2012) 3025–3033.
- [23] H. Vrubel, X. Hu, *Angew. Chem. Int. Ed.* 51 (2012) 12703–12706.
- [24] Y. Zheng, Y. Jiao, Y. Zhu, L.H. Li, Y. Han, Y. Chen, A. Du, M. Jaroniec, S.Z. Qiao, *Nat. Commun.* 5 (2014) 3783.
- [25] J. Rosen, G.S. Hutchings, F. Jiao, *J. Am. Chem. Soc.* 135 (2013) 4516–4521.
- [26] G.S. Hutchings, Y. Zhang, J. Li, B.T. Yonemoto, X. Zhou, K. Zhu, F. Jiao, *J. Am. Chem. Soc.* 137 (2015) 4223–4229.
- [27] D.K. Bediako, Y. Surendranath, D.G. Nocera, *J. Am. Chem. Soc.* 135 (2013) 3662–3674.
- [28] K. Fominykh, J.M. Feckl, J. Sicklinger, M. Döblinger, S. Böcklein, J. Ziegler, L. Peter, J. Rathousky, E.-W. Scheidt, T. Bein, D. Fattakhova-Rohlfing, *Adv. Funct. Mater.* 24 (2014) 3123–3129.
- [29] F. Song, X. Hu, *J. Am. Chem. Soc.* 136 (2014) 16481–16484.
- [30] M. Huynh, D.K. Bediako, D.G. Nocera, *J. Am. Chem. Soc.* 136 (2014) 6002–6010.
- [31] L. Trottochaud, S.L. Young, J.K. Ranney, S.W. Boettcher, *J. Am. Chem. Soc.* 136 (2014) 6744–6753.
- [32] Juan F. Callejas, Joshua M. McEnaney, Carlos G. Read, J. Chance Crompton, Adam J. Biacchi, Eric J. Popczun, Thomas R. Gordon, Nathan S. Lewis, R.E. Schaak, *ACS Nano* 8 (2014) 11101–11107.
- [33] C.G. Morales-Guio, S.D. Tilley, H. Vrubel, M. Gratzel, X. Hu, *Nat. Commun.* 5 (2014) 3059.
- [34] Z. Chen, T.J. Meyer, *Angew. Chem. Int. Ed.* 52 (2013) 700–703.
- [35] S. Cobo, J. Heidkamp, P.A. Jacques, J. Fize, V. Fourmond, L. Guetaz, B. Jousselme, V. Ivanova, H. Dau, S. Palacin, M. Fontecave, V. Artero, *Nat. Mater.* 11 (2012) 802–807.
- [36] C. He, X. Wu, Z. He, *J. Phys. Chem. C* 118 (2014) 4578–4584.
- [37] L.-A. Stern, L. Feng, F. Song, X. Hu, *Energy Environ. Sci.* 8 (2015) 2347–2351.
- [38] H. Jin, J. Wang, D. Su, Z. Wei, Z. Pang, Y. Wang, *J. Am. Chem. Soc.* 137 (2015) 2688–2694.
- [39] D. Liu, Q. Lu, Y. Luo, X. Sun, A.M. Asiri, *Nanoscale* 7 (2015) 15122–15126.
- [40] P. Jiang, Q. Liu, X. Sun, *Nanoscale* 6 (2014) 13440–13445.
- [41] L. Feng, H. Vrubel, M. Bensimon, X. Hu, *Phys. Chem. Chem. Phys.* 16 (2014) 5917–5921.
- [42] M. Ledendecker, S. Krick Calderon, C. Papp, H.P. Steinruck, M. Antonietti, M. Shalom, *Angew. Chem. Int. Ed.* 127 (2015) 12538–12542.
- [43] Z. Huang, Z. Chen, Z. Chen, C. Lv, H. Meng, C. Zhang, *ACS Nano* 8 (2014) 8121–8129.
- [44] J. Chang, S. Li, G. Li, J. Ge, C. Liu, W. Xing, *J. Mater. Chem. A* 4 (2016) 9755–9759.
- [45] Y. Ni, A. Tao, G. Hu, X. Cao, X. Wei, Z. Yang, *Nanotechnology* 17 (2006) 5013–5018.
- [46] J. Chang, Y. Xiao, M. Xiao, J. Ge, C. Liu, W. Xing, *ACS. Catal.* 5 (2015) 6874–6878.
- [47] Y. Leng, G. Chen, A.J. Mendoza, T.B. Tighe, M.A. Hickner, C.Y. Wang, *J. Am. Chem. Soc.* 134 (2012) 9054–9057.
- [48] M. Xiao, J. Zhu, J. Ge, C. Liu, W. Xing, *J. Power Sources* 281 (2015) 34–43.
- [49] A.R.J. Kucernak, V.N. Naranamalpuram Sundaram, *J. Mater. Chem. A* 2 (2014) 17435–17445.
- [50] Y. Pan, Y. Liu, J. Zhao, K. Yang, J. Liang, D. Liu, W. Hu, D. Liu, Y. Liu, C. Liu, *J. Mater. Chem. A* 3 (2015) 1656–1665.
- [51] R.D. Smith, M.S. Prevot, R.D. Fagan, S. Trudel, C.P. Berlinguette, *J. Am. Chem. Soc.* 135 (2013) 11580–11586.
- [52] M.W. Louie, A.T. Bell, *J. Am. Chem. Soc.* 135 (2013) 12329–12337.
- [53] Y. Yang, H. Fei, G. Ruan, J.M. Tour, *Adv. Mater.* 27 (2015) 3175–3180.
- [54] J. Chang, L. Liang, C. Li, M. Wang, J. Ge, C. Liu, W. Xing, *Green Chem.* 18 (2016) 2287–2295.
- [55] H.S. Ahn, A.J. Bard, *J. Am. Chem. Soc.* 137 (2015) 612–615.
- [56] R. Wu, J. Zhang, Y. Shi, D. Liu, B. Zhang, *J. Am. Chem. Soc.* 137 (2015) 6983–6986.